# Network of thermal cracks in meteorites due to temperature variations: new experimental evidence and implications for asteroid surfaces

Guy Libourel, Clément Ganino, Marco Delbo, Mathieu Niezgoda, Benjamin Rémy, Lionel Aranda, Patrick Michel

Monthly Notices
of the
ROYAL ASTRONOMICAL SOCIETY

MNRAS **500,** 1905–1920 (2021)
Advance Access publication 2020 October 22

doi:10.1093/mnras/staa3183

# Network of thermal cracks in meteorites due to temperature variations: new experimental evidence and implications for asteroid surfaces

Guy Libourel,[1,2]★ Clément Ganino,[3] Marco Delbo,[1] Mathieu Niezgoda,[4] Benjamin Remy,[5] Lionel Aranda[6] and Patrick Michel[1]

[1]*Observatoire de la Côte d'Azur, CNRS, Laboratoire Lagrange, Université Côte d'Azur, UMR 7293, Boulevard de l'Observatoire, CS 34229, F-06304 Nice Cedex 4, France*
[2]*School of Ocean, Earth Science and Technology, Hawai'i Institute of Geophysics and Planetology, University of Hawai'i at Mānoa, Honolulu, HI 96821, USA*
[3]*Observatoire de la Côte d'Azur, CNRS, Laboratoire Géoazur, Université Côte d'Azur, 250 rue Albert Einstein, Sophia-Antipolis, F-06560 Valbonne, France*
[4]*Commissariat à l'Energie Atomique et aux Energies Alternatives, CEA/DES/ISAS/DM2S/STMF/LMEC, PC 47, F-91191 Gif-sur-Yvette cedex, France*
[5]*Université de Lorraine, Laboratoire d'Energétique et de Mécanique Théorique Appliquée, CNRS, UMR 7563, 2 avenue de la Forêt de Haye, TSA 60604, F-54518 Vandoeuvre-les-Nancy Cedex, France*
[6]*Département Chimie et Physique des Solides et des Surfaces, Institut Jean Lamour, Université de Lorraine, UMR 7198, F-54000 Nancy, France*

Accepted 2020 September 21. Received 2020 September 21; in original form 2020 July 2

## ABSTRACT

In recent years, several studies have shown the importance of thermal fracturing of rocks due to temperature variations, on The Earth and Mars. Rock thermal cracking might also be a process at play on the lunar surface. These temperature variations as well as change rates can reach important amplitude on bodies without an atmosphere, in particular on those that reach small perihelion distances such as near-Earth asteroids. On the other hand, the formation, geometry, and extension of cracks on these bodies have not been fully investigated yet. Here, we show results of thermal cracking laboratory experiments on chondrite meteorites, which develop networks of cracks when subjected to rapid temperature cycles with amplitudes similar to those experienced by asteroids with low perihelion distances. The depth of the cracks can reach a few hundred of microns in some hundreds of temperature cycles, in agreement with theoretical studies. We find that dehydration of hydrous minerals enhances the cracking process. The formation of crack networks increases the porosity both at the surface and in the sub-surface of our specimens. We propose that this process could help explaining the recent finding of the very highly porous surfaces of most of the boulders on the asteroids Ryugu and Bennu.

**Key words:** meteorites, meteors, meteoroid – minor planets, asteroids: general.

## 1 INTRODUCTION

Regolith, which literally means a blanket of rocks, is a layer of more or less loose unconsolidated and usually fine debris (with sizes ranging from few microns to few cm) that can be found on the surface of several planetary bodies. Our moon, for instance, has thick and fine regolith with particle sizes typically ranging from a few millimetres to a few tens of microns (Heiken & McKay 1974). On the other hand, on different asteroids, space exploration missions have shown that regolith can be dramatically different. For instance, the ∼100 km-sized asteroid (21) Lutetia is also covered by thick and abundant fine regolith (Vincent et al. 2012, Gundlach & Blum 2013); the near-Earth asteroid (433) Eros has been shown to have coarser regolith than our Moon, with typically mm-sized and larger particles (Veverka et al. 2001). The near-Earth asteroid (25 143) Itokawa, with an equivalent spherical diameter of only 350 m, displays an even coarser regolith than Eros, with typical grain size of centimetres (Yano et al. 2006). On this latter asteroid, the finer component of the regolith is not widespread, but it is essentially confined in gravitational potential lows probably due to migration (Miyamoto et al. 2007). Boulders with sizes up to several meters dominate areas where fine regolith is apparently lacking (Tsuchiyama et al. 2008). The recent observations obtained by NASA's OSIRS-REx and JAXA's Hayabusa2 missions of near-Earth asteroids (101 955) Bennu and (162 173) Ryugu challenged the paradigm that fine regolith is in general present on asteroids: *in situ* images reveal rugged surfaces almost entirely dominated by boulders (Walsh et al. 2019; Watanabe et al. 2019; Molaro et al 2020), except in some specific places, such as the sampling site candidates of OSIRIS-REx on Bennu.

On the Moon, regolith generation has traditionally been attributed to the break-up of boulders exposed on the surface to micrometeoroid impacts (Housen et al. 1979; Hörz & Cintala 1997). As boulders are comminuted over the eons, fresh ones need to be emplaced on the surface by the fallback of the ejecta of craters formed by impacts that penetrated the bedrock underlying the regolith blanket (Housen et al. 1979; Hörz & Cintala 1997). Recent analysis of LROC/NAC images of *in situ* fractured lunar boulders, observed on the rim of impact craters, shows that the relative number of disrupted blocks increases with crater-retention age of surfaces on which blocks are hosted (Ruesch et al. 2020). This is consistent with fragmentation post-emplacement due to impacts of small meteoroids (Ruesch et al. 2020), confirming the regolith formation process from boulder comminution. This work also shows that the possible effects of

★ E-mail: libou@oca.eu

insolation-driven thermal stresses are evident as meridional cracks, which have preferred orientations in young block populations.

On asteroids, regolith production by the break-up of boulders due to micrometeoroid impacts is frustrated by the low escape velocities from these bodies compared to typical ejecta speed produced by hypervelocity impacts (Housen et al. 1979; Housen & Holsapple 2011), although the observation of the ejecta cloud from the impact of the Hayabusa2 Small Carry-on Impactor on Ryugu showed that low-speed ejecta can be produced and fall back on a small asteroid surface (Arakawa et al. 2020). It is also likely that micrometeoroid impacts are able to kick out boulders of a few decimeters in size from small asteroid surfaces: this process has been suggested among others for the activity observed by the OSIRIS-REx mission on the asteroid Bennu (Lauretta et al. 2019). However, Dombard et al. (2010) noticed that several boulders inside craters on Eros' surface erode in place, creating 'ponds' of fine regolith materials that fill the crater floor. The same authors claim that thermal stresses due to day–night temperature variations could be the driving force causing said boulder erosion. Delbo et al. (2014) showed that temperature oscillations with amplitudes of some tens to 100° and period of a few hours create mechanical stresses in meteorite specimens capable of driving crack propagation. These temperature variations are typical of those caused by diurnal insolation cycles on asteroids (Delbo et al. 2014). Independent modelling reached similar conclusions, namely that thermally driven stresses lead to cracking of asteroid surface rocks (Molaro Byrne & Le 2017). In addition, OSIRS-REx Polycam observations, at a spatial resolution of some cm, show that several boulders on the surface of Bennu display fractures and morphologies compatible with an exfoliation process (Molaro et al. 2020). The same authors perform a thermo–elastical modelling of the observed boulders, which indicate that the aforementioned features are consistent with the result of releasing stresses generated by temperature cycling. In those conditions, when thermal stress values are smaller than the strength of the rock, the latter experiences sub-critical crack growth, meaning that the crack length increases by a tiny amount at each temperature cycles (see e.g. extended data fig. 7 of Delbo et al. 2014). We call this case thermal fatigue, which can lead to damage and possibly rock fragmentation when the number of cycles is very large. When the crack growth measured by Delbo et al. (2014) is extrapolated over the ages of asteroids, it is conceivable that crack growth could cause the chipping of boulder surfaces or the breaking of surface rocks, thus producing fresh regolith (Delbo et al. 2014; Hazeli et al. 2018; El-Mir et al. 2019; Ravaji et al. 2019). A volumetric stress analysis as function mechanical and thermal loadings in a L6 ordinary chondrite based on experimental data (Liang et al. 2020) has recently shown that the stress concentrates more uniformly in matrix-particle interfacial regions, resulting in the particle debonding from the surrounding matrix.

Thermal fatigue is also inferred to be the mechanism responsible for the propagation of fractures observed by the instruments of the ESA space mission Rosetta on the nucleus of the comet 67P/Churyumov–Gerasimenko (El-Maarry et al. 2015; Vincent et al. 2015), and possibly the onset of the early activity of the comet (Alí-Lagoa Delbo & Libourel 2015). Thermally driven stresses are shown to be at the origin of polygonal fractures observed in several areas of the nucleus of 67P/Churyumov–Gerasimenko (Auger et al. 2018). Thermomechanical modelling indicates that temperature-driven thermal fracturing may be an important erosion process on cometary surfaces, which breaks down material and weakens cliffs (Attree et al. 2018). In particular, a spectacular cliff break-down and collapse probably assisted by thermal stress cycling was observed by Rosetta on the nucleus of the comet 67P/Churyumov–Gerasimenko (Pajola et al. 2017).

While thermal stress weathering is now considered a significant process at play on airless solar system bodies orbiting the sun with distances of some astronomical units, its importance on planets with atmosphere, such as the Earth and Mars, has been revived by recent studies: Collins & Stock (2016) measured crack propagation on a rocky slab on an exfoliating granite cliff in Yosemite National Park in California, USA, clearly correlated with diurnal and seasonal temperature oscillations. The same authors apply a fracture propagation model to interpret their data and conclude that cyclic thermal stressing is driving exfoliation fractures, eventually leading to rockfall in Yosemite National Park. Collins et al. (2018) also correlated temperature oscillations and spontaneous rock exfoliation in a rock dome in California. Viles et al. (2010) submitted in the laboratory martian-type basalts to temperature cyclic variations similar to those occurring on the red planet and measured a weakening of the rock strength as a result of these cycles. The weakening of the specimens could be related to the growth of cracks within the materials, a typical result of thermal fatigue. Eppes et al. (2015) demonstrated that fractures in Martian boulders, measured along the exploration path of the Spirit rover (NASA), exhibit preferred orientations that point to solar-induced thermal stress, as observed on the Moon (Ruesch et al. 2020).

Despite significant progress in the two last decades, we still only partly understand how regolith forms at the surface of asteroids and the extent to which it is altered from its pristine conditions by exposure to space, an information that is critical for interpreting the data collected by space missions. For example, does regolith form in the same way on all surfaces and conditions or does its formation change with time, composition, and location in the solar system? Is there a difference in the regolith particles produced by thermal cracking and those created by impacts? In the framework of regolith formation studies via thermal cracking, it is also important to understand and quantify the process of selective asteroid disintegration near the sun reported by Granvik et al. (2016). These authors show a significant lack of low-albedo and low-perihelion near-Earth asteroids, which could be explained by a steady thermal disintegration of their surfaces.

For all the reasons above, and following the work of Delbo et al. (2014) on the effect of thermal cycling on the cracking of chondrites, used as proxies of asteroidal materials, we have undertaken a new series of experiments at higher dT/dt (where T is the temperature and t is the time) to evaluate the effect of the number of cycles and the nature/composition of the starting materials on crack formation and growth. Our experiments at higher temperature excursion and higher temperature rate of changes are also more appropriate for low perihelion near-Earth asteroids than those carried out by Delbo et al (2014). In the following, we describe the experimental set-up and protocol; next we present the results of our experiments. We shall see how thermal cycling activates pre-existing generation of flaws and cracks by favouring crack propagations. We will also show the important role of hydrous minerals on the propagation of cracks and the modification of the outer layer surface porosity of our specimens. Implications of these results are then discussed in a planetary science perspective.

## 2 EXPERIMENTAL, METHODS, AND STRATEGY

To consider the diversity of asteroid surfaces, thermal cycling experiments were undertaken on three different cm-sized chondrite

samples, each used as a proxy of a specific asteroid composition: two carbonaceous chondrites, namely Murchison CM2 and Allende CV3, and the Sahara 97 210, L/LL3.2 ordinary chondrite. Like most carbonaceous Mighei-type chondrites, Murchison is of petrologic type 2, which means that it experienced extensive alteration by water-rich fluids on its parent body (likely at times >4.5 Gyr ago) before falling to The Earth. By comparison, Allende (type 3), belonging to the carbonaceous Vigarano-type chondrite group, is less weathered (aqueous altered). Sahara 97 210 differs significantly from the two other lithologies by having a very low matrix/chondrule ratio (<0.1) and almost no hydrous phases, as ordinary chondrites generally do.

This diversity also results in very different physical properties. Carbonaceous chondrites have much lower bulk densities and higher porosities than ordinary ones, e.g. density of 2.12 ± 0.26 g.cm$^{-3}$, 2.95 ± 0.26 g.cm$^{-3}$, 3.21 ± 0.22 g.cm$^{-3}$ and porosity of 23.0 ± 7.5 per cent, 13.8 ± 9.1 per cent, 7.9 ± 4.2 per cent, respectively, for CM, CV, and OC type L (Britt & Consolmagno 2003). The grain density also displays a large range from 2.71 ± 0.11 g.cm$^{-3}$ for CM to 3.48 ± 0.09 g.cm$^{-3}$ for CV and 3.51 ± 0.11 g.cm$^{-3}$ for L chondrites (Britt & Consolmagno 2003). The low grain density of CM and especially Murchison is related to the high matrix proportion and to the modal abundances of phyllosilicates. Their mechanical properties differ too, Murchison being friable with a tensile strength of ∼2 ± 1.5 MPa (Tsuchiyama et al. 2008), Allende's tensile strength is approximately 28 MPa in its currently compressed form (Svetsov Nemtchinov & Teterev 1995), while ordinary chondrites have average values between 18 and 31 MPa (Slyuta 2017; Polh & Britt 2020). As shown by the choice of our experimental conditions (Table 1), we produced a large number of experiments with duplicates in order to ensure reproducibility and have as much as possible an unbiased data set for depicting the effect of thermal cycling on our representative chondrite samples.

To begin with, a series of thermo-gravimetric analysis (TGA) experiments was undertaken to characterize the behaviour of the specimens in term of volatile release with increasing temperature. A thermogravimeter (Setsys Ev 1750 TGA, SETARAM) coupled with a mass spectrometer (Omnistar GSD 301C, Pfeiffer Vacuum) at Institut Jean Lamour (Nancy, France) have been used. Samples of 16.20, 46.65, and 61.22 mg for Murchison, Allende, and Sahara 97 210, respectively, were exposed to a progressive heating temperature from 193 to 1373 K with a ramp 5 K min-1 under He atmosphere. TGA was used to quantify the amount of volatile elements in the samples by measuring the mass-loss as a function of heating. The first derivative (DTG) of the TGA curve enabled us to determine the maximum peak temperature of each mass-loss and gives an indication of the host mineral of volatile elements.

Concerning the protocol for thermal cycling, in the previous experimental work of Delbo et al. (2014) a climatic chamber was used to subject meteorite samples to temperature cycles in dry atmosphere at a pressure of 1 bar; the temperature cycle period was 2.2 h; the temperature excursion (peak to peak) was $\Delta T \approx 190$ K with a $T_{max} \approx 440$ K; the temperature rate of change was dT/dt ≈ 4 K min$^{-1}$, corresponding to the highest heating rate of this climatic chamber; and the number of the temperature cycles was of the order of 400.

Here, in order to enhance the effects of thermal cycles and apply different dT/dt on different meteorite compositions, samples were heated in air, starting from room temperature, by a continuous $CO_2$ laser emitting in the infrared at a wavelength of 10.6 μm with a power of 130 W (Fig. 1). An electro-optical switch was used to enable and cut the laser power in order to regulate the heating time of the sample. The cooling of the sample was passive, driven by the ambient air and the contact of the face opposite to the laser beam with the sample holder. The laser beam diameter was 6 mm at the specimen (beam divergence was of 4.5 μrad.) Samples are located on a sample holder at an angle of 45° from the perpendicular plan to the firing laser beam line, allowing us to observe specimen's front face with an infrared camera (Cedip/FLIRr). The camera had a InSb 640 × 512 detector matrix, cooled at 77 K via a Stirling-cycle compressor. The Noise-Equivalent Temperature Difference, which is a measure for how well a thermal imaging detector is able to distinguish between very small differences in temperature on the image, was of 25 mK at ambient temperature. The time of acquisition (timeliness of photons collection) was chosen to be 750 μs. The chosen objective for this experiment had a focal length of 72 mm with an extension ring of 5 mm, so that samples cover most of the field seen by the camera. This camera was directly calibrated in temperature such that the pixel values in the images acquired by a computer correspond directly to temperatures (in K). This set-up allowed monitoring accurately the temperature of the surface of our samples during the temperature cycling.

Samples were exposed to temperature cycle periods of 40 s, split into 400 ms of heating then 39.6 s of cooling, with $\Delta T \approx 280$ K and corresponding $T_{max} \approx 583$ K or $\Delta T \approx 530$ K and $T_{max} \approx 713$ K. The dT/dt was >> 4 K min$^{-1}$ in all cases and we performed a number of cycles up to 1500 (Table 1). The magnitude of the temperature excursion was selected to be circa 300–350 K, a range almost equal to the ΔT diurnal surface temperature excursions of C-type asteroids at 0.5 au from the Sun (see Delbo et al. 2014, Methods and Extended Data Fig. 2). The effect of thermal cycling being very tenuous for Sahara 97 210 samples, a series of thermal cycling experiments has been carried out at a maximum temperature of 713 K and $\Delta T \approx 530$ K (Table 1). In general, the embrittlement in rock samples is related to heating rates. Richter & Simmons (1974) claimed that almost no crack propagation was detected at rates <2 K min$^{-1}$. Although this dT/dt value is no longer considered as an absolute threshold to have or not to have thermal cracking (Molaro et al. 2017; Ravaji et al. 2019), it is clear that high values of temperature rates of change are likely to propagate cracks in brittle materials. In essence, thermal stresses in unconstrained bodies arise when the spatial second derivative of the temperature is non-negligible (Ravaji et al. 2019). But the latter is related – via the heat diffusion equation – to dT/dt (Ravaji et al. 2019). Here, much higher dT/dt values >> 2 K min$^{-1}$ have been imposed, which are likely in the crack propagation domain for meteorites. Such heating rates, necessary for a high number of short cycles at laboratory time-scales, surpass those expected in most planetary environments, except perhaps those related to some rapid shadowing events occurring on irregular surfaces (e.g. Bennu, Ryugu), and any conclusion on the necessary number of cycles to cause embrittlement and crack propagation in natural conditions cannot be drawn from this data set. However, the main objective here was instead to characterize the relative effect of thermal cycling on various chondrite surfaces both at low and high number of cycles and to reveal the mechanism of crack formation and growth everything being equal for each chondrite sample. In planetary perspective, this study should be considered as a proof of concept-like experiments rather than a quantitative analysis of the effect of thermal loading on crack growth and formation of crack networks.

In order to characterize the evolution of samples as a function of the thermal cycling imposed by the laser pulses, 2–3-cm-sized samples have been polished on both sides (thickness 5–10 mm). This allows us to observe crack formation and propagation using scanning electron microscopy (SEM). After a given number of cycles (0, 2, 4, 8, 16, 32, etc.), the samples were taken down from the laser- and camera-equipped optical bench and moved

**Table 1.** Thermal cycling experimental run conditions. Chondrite samples were exposed to temperature cycle periods of 40 s, with $\Delta T \approx 280$ K and $T_{max.} \approx 583$ K. Each cycle corresponds to 400 ms of heating then 39.6 s of cooling. For each thermal cycle, estimated dT/dt on heating is on the order of 800 and of 8 K $s^{-1}$ on cooling. Only Sahara 97 210 sample was exposed to temperature cycle of $\Delta T \approx 530$ K and $T_{max.} \approx 713$ K.

| | Allende | | | Murchison | | | | Sahara 97 210 | | |
|---|---|---|---|---|---|---|---|---|---|---|
| | Cycles | SEM | Tomography | Cycles | SEM | Tomography | | Cycles | SEM | Tomography |
| **Experiment 1** | | | | | | | | | | |
| Initial | | x | | | x | | Initial | | x | |
| 100 cycles | x | x | | x | x | | 100 cycles | x ($\Delta T \approx 530$ K) | x | |
| 300 cycles | x | x | x | | | | | | | |
| 700 cycles | x | x | | | | | | | | |
| 1000 cycles | x | x | x | | | | | | | |
| 1500 cycles | x | x | | | | | | | | |
| **Experiment 2** | | | | | | | | | | |
| Initial | | x | x | | x | x | Initial | | x | |
| 1 cycle | x | x | | x | x | | 2 cycles | x | x | |
| 2 cycles | x | x | | x | x | | 8 cycles | x | x | |
| 4 cycles | x | x | | x | x | | 16 cycles | x | x | |
| 8 cycles | x | x | | x | x | | 32 cycles | x | x | |
| 16 cycles | x | x | | x | x | | 64 cycles | x | x | |
| 32 cycles | x | x | | x | x | | 128 cycles | x | x | |
| 64 cycles | x | x | x | x | x | x | 256 cycles | x | x | |
| 128 cycles | x | x | x | x | x | x | 512 cycles | x | x | |

to the SEM. Note that the same sample has been used in this experimental procedure. Caution was taken in re-mounting samples in the same positions such that the laser shots were focused at the same location on each sample surface all the time. SEM and Energy Dispersive X-ray (EDX) spectral analyses were performed on each selected ran samples at Centre de Recherches Pétrographiques et Géochimiques (CRPG-CNRS; Nancy, France) using a JEOL JSM-6510 equipped with an EDX Genesis X-ray detector, using a 3 nA primary beam at 15 kV. Complementary to these aforementioned 2D SEM surface observations, we performed on a few ran samples an X-ray 3D tomography in order to characterize crack propagation and crack structure at depth. The X-ray 3D tomography was performed using a Phoenix Nanotom (X-ray tube 180 kV/15 W) from the Service Commun de Microscopies Electroniques et de Microanalyses (SCMEM; Université de Lorraine, France).

SEM images were processed using imageJ to quantify the proportion of cracked surface through time. The first step was to adjust brightness/contrast to improve the visual crack identification. The second step was to apply a threshold to keep only the darkest part of the image, including the cracks. The third and last step was to clean manually all the dark particles that remained and were clearly unrelated to cracks after the thresholding. After this processing, we obtained a binary (black and white) image on which it was possible to count the ratio between the number of black pixels (corresponding to cracks) and the total number of pixels in the image. As this procedure was not fully automatic, the area of crack detected depends on the user. In order to estimate variability associated with the tuning of brightness/contrast adjustment to the threshold and to the manual cleaning, we fully processed five times one image for each experiment and calculated the standard deviation.

## 3 RESULTS

### 3.1 Thermogravimetry analyses

Expectedly, the mass change upon thermogravimetry experiments differs significantly between Murchison (CM2), Allende (CV3), and Sahara 97 210 (L/LL3.2) samples (Fig. 2a). Upon heating from room temperature up to 1373 K, Murchison reached ∼15 per cent weight lost, Allende around ∼4 per cent while Sahara 97 210 shows no significant variation (<0.16 per cent): see Fig. 1(a). When limited to the temperature range of our thermal cycling experiments the trend is identical, with Murchison having lost 3.26 per cent at 483 K, Allende having lost 2.18 per cent at 413 K and Sahara having lost a limited amount of 0.05 per cent at 483 K reaching only 0.1 per cent for experiment 5 and thermal cycling up to 713 K. The correlation between mass-loss and amount of volatile-rich phases in these chondrites is obvious and will be discussed below. The first derivative (DTG) of the TGA curve enables us to determine the maximum peak temperature of each mass-loss and gives an indication of the host mineral of volatile elements (Fig. 2b). Previous studies using standards (Garenne et al. 2014 and references therein) have shown that (i) the mass-loss between 300 and 473 K is mainly due to the release of adsorbed $H_2O$ molecules (molecular water) and mesopore water, (ii) the mass-loss between 473 and 673 K is attributed to the release of $H_2O$ from (oxy)-hydroxide minerals, and (iii) the release of hydroxyl groups (–OH) from phyllosilicates is in the range of 673–1043 K. Mass-loss at higher temperature in the range of 1050–1200 K could be attributed to carbonate and/or sulfate degassing. Accordingly, the DTG curve can be used as an indicator of the mineralogy of hydrous phases by identification of peak position as a function of temperature (Garenne et al. 2014).

The DTG curves for the studied chondrites are consistent with their documented bulk mineralogy. Murchison reached a ∼15 per cent weight lost, consistent with Garenne et al. (2014) data, which is mostly related to the release of water from hydrous minerals (∼72 per cent of hydrous minerals, Howard et al. 2009) and the volatilization of carbon and sulfur (∼1.8–4.1 per cent, Gibson Jr 1976). Allende (CV3) displayed a mass-loss limited to ∼4 per cent at the end of the heating experiment in good agreement with the scarce amount of hydrous phase (Howard et al. 2010). Finally, the DTG of LL3 chondrite Sahara 97 210 shows very little variation in the studied range of temperature values suggesting

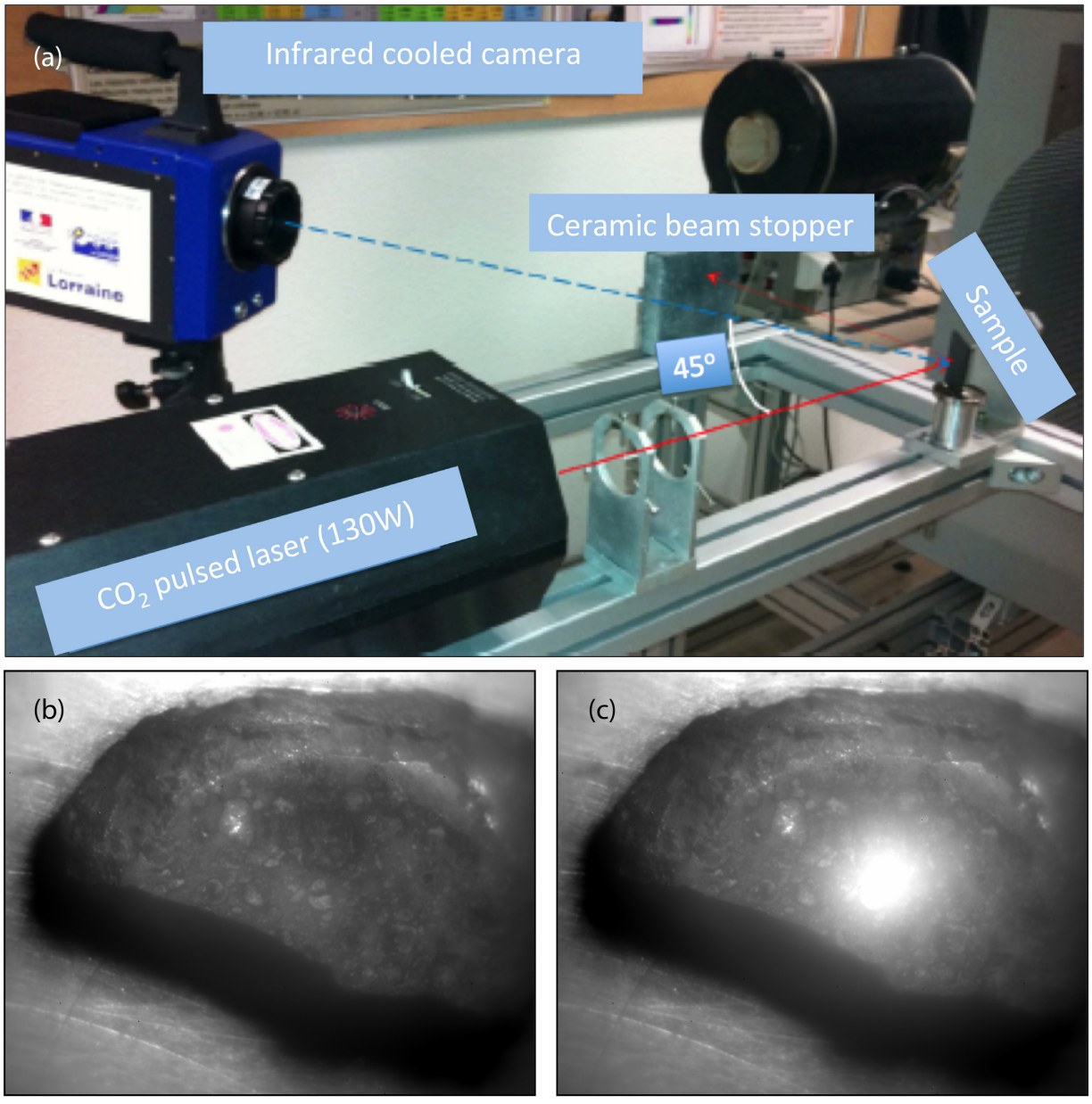


**Figure 1.** (a) Thermal cycling experimental set-up using a continuous $CO_2$ laser emitting in the infrared. 3.5-cm-sized Allende sample prior (b) and during (c) the laser heating pulse. The laser beam diameter, as seen by the IR camera in (c), was around 6 mm at the specimen surface.

the almost total absence of hydrous phases. For the maximum temperature reached in these sets of thermal cycling experiments where $T_{max}$ ~500 K, DTG curves clearly indicate that the main mass-loss is due to a (thermal) dehydration process corresponding to the release of molecular water and in a lesser extent to the release of $H_2O$ from (oxy)-hydroxide minerals whatever the chondrite type is considered. Apparently no dehydroxylation process of phyllosilicates seems to be involved at a temperature below ≈ 500 K; dehydroxylation being defined as the heating process at a temperature above ≈ 600–700 K (Fig. 2b) through which the hydroxyl group (-OH) is released by forming a water molecule and causing a significant change in volume of the mineral (see below).

### 3.2 Thermal cycling and the origin of network of cracks

In this set of laser-induced thermal cycling experiments, the large amplitude of the temperature excursion associated with a high dT/dt and the large number of thermal cycles performed were at the origin of the formation and development of remarkable networks of cracks (Figs 3 and 4). For instance, Fig. 3 shows the network of cracks of the Allende surface sample after a series of 1000 thermal cycles. It is important to note that the network of cracks developed only in the region affected by the laser.

Fig. 4 shows another example of the surface of Murchison with a dense network of cracks developed after only 100 thermal cycles (Table 1). For this experiment $T_{max}$ was 583 K. For similar conditions

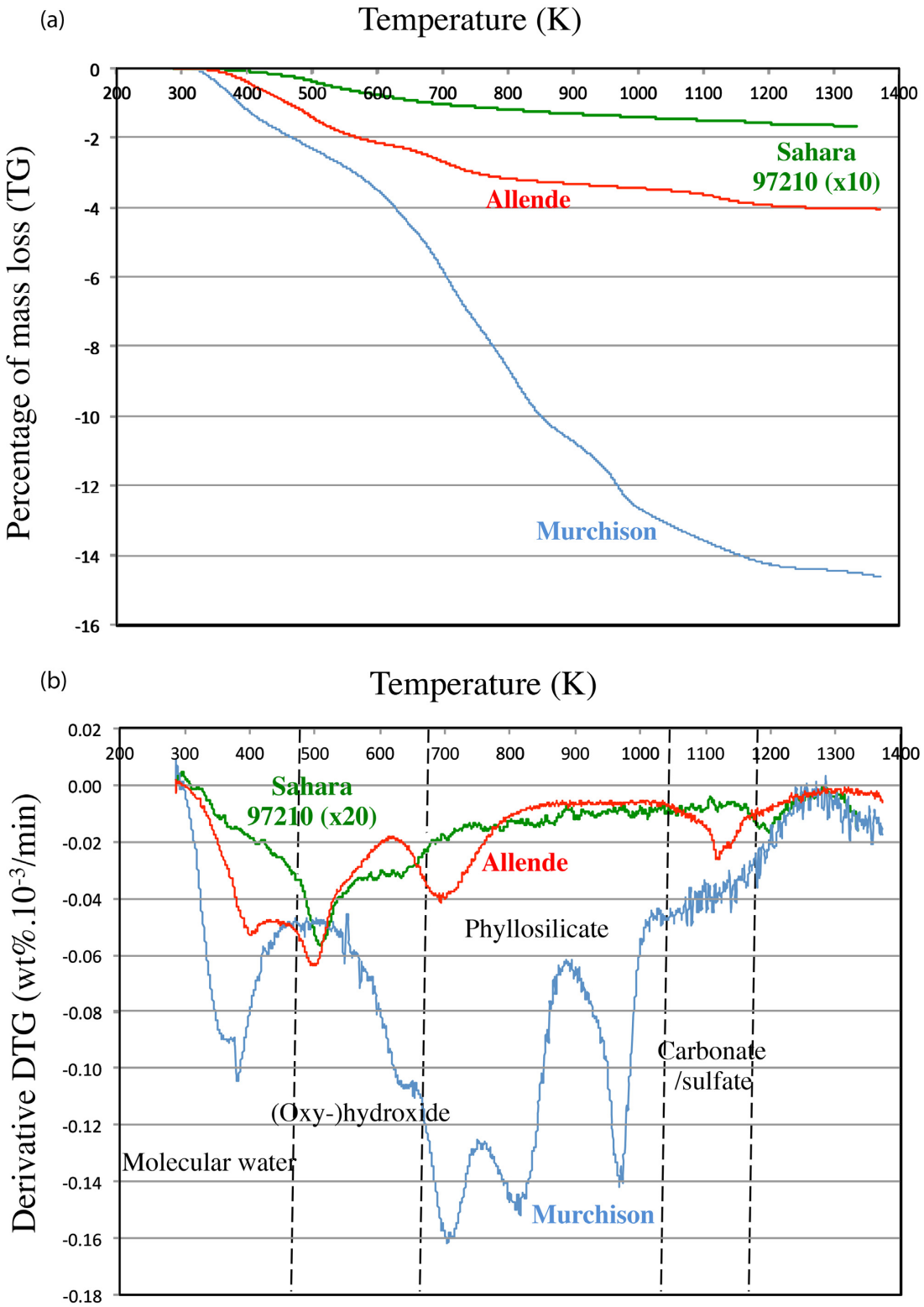


**Figure 2.** Thermogravimetric analysis (TGA) curve (a) and the first derivative (DTG) of the TGA curve (b) for Allende, Murchison and Sahara 97 210 samples. The decomposition of the TGA curve in different types of mineralogy as a function of temperature (Garenne et al. 2014) is also shown.

of thermal cycling, the crack growth differs significantly depending on the studied chondrite group and its efficiency is increasing from Sahara 97 210 (OC), to Allende CV3, to Murchison CM, with the latter showing a dramatic increase compared to the other specimens (Figs 5–7). Cracks are very thin and difficult to recognize in the OC chondrite (Fig. 7), whereas Murchison CM thermal cycled samples (Fig. 5) show large cracks, a few tens of microns wide, constituting marked and highly visible networks (Fig. 8). The Allende CV3

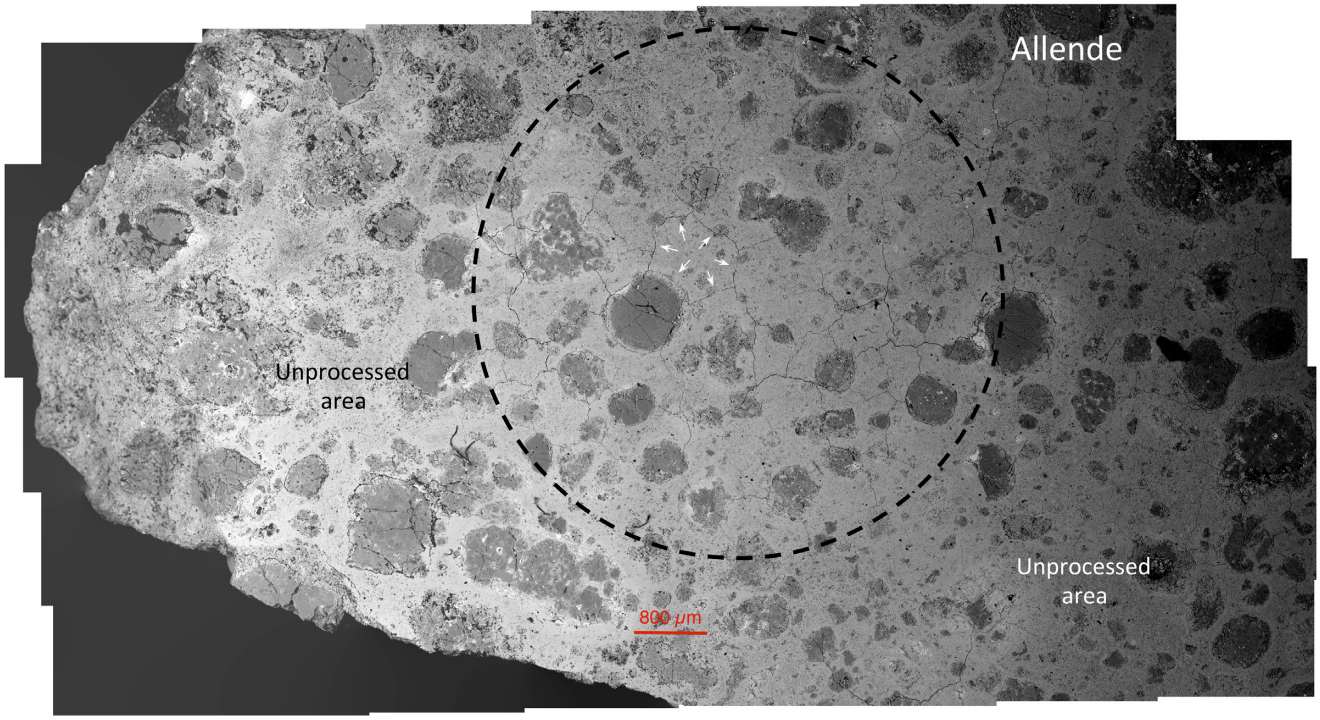


**Figure 3.** EDS–SEM image showing an example of network of cracks obtained on a polished Allende surface after a series of 1000 thermal cycles ($\Delta T \approx 280$ K and $T_{max.} \approx 583$ K). Belonging to CV3 chondrites, this section is composed of a fine-grained olivine (fayalite 50) dominated matrix in which are dispersed millimetre-sized chondrules. The dashed circle delineated approximately the ∼6 mm laser beam size. Note that the network of cracks, well centered on laser spot, is surrounded by unfractured/unprocessed area. Cracks develop segments that propagate in the chondrite matrix, across chondrules and in some case around chondrules. As an example, the white arrows outline cracks delineating a polygonal-structure made by six crack segments.

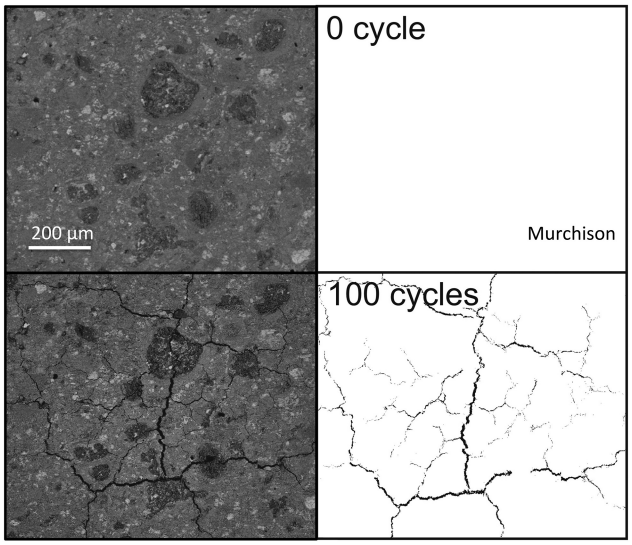


**Figure 4.** EDS–SEM images of the surface of Murchison (CM2) before (0 cycle) and after 100 thermal cycles (($\Delta T \approx 280$ K and $T_{max.} \approx 583$ K). Chondrules in Murchison are smaller than those of CV3 carbonaceous chondrites. In contrast to Allende and Sahara 97 210, Murchison matrix is richer in phyllosilicates and other hydrous phases. Cracks propagate indifferently in the chondrite matrice or across chondrules.

chondrite sample (Fig. 6) displays a crack network that is in between the two extreme cases of Murchison and Sahara 97 210 in terms of extension and width of cracks. On average, crack width increases drastically from Sahara 97 210 (<5 µm), Allende (≈ 5–10 µm), and Murchison (up to 40–50 µm).

With increasing the number of cycles in all experiments, cracks develop forming segments that propagate in the chondrite matrices or across chondrules (Figs 3 and 4). The propagation through chondrules is somehow unexpected, as previous studies indicated that the maximum stress is localized at the interfaces between the chondrules and the matrix, ideally leading to crack propagation along these interfaces (Molaro Byrne & Langer 2015; Hazeli et al. 2018). In thermal cycling experiments using Allende and Murchison as samples, some fractures get around chondrules, which should facilitate the enucleation of chondrules from their chondritic matrix (Fig. 3), a behaviour that is expected from theory (Molaro et al. 2015) and experiments (Hazeli et al. 2018). A recent *in situ* 3D investigation of ordinary chondrite (Liang et. al. 2020) under thermal cycling and mechanical loading is also consistent with these previous theoretical and experimental findings (Molaro et al. 2015; Hazeli et al. 2018) and shows that under thermal loading crack concentrates preferentially in matrix-particle interfacial regions. At larger SEM magnification, a crack network with some fractal characteristics is visible in Murchison sample (Fig. 8). Similar features are found in Allende and Sahara 97 210 at large numbers of thermal cycles (Figs 3 and 9).

### 3.3 Crack growth rates

We evaluated the relative crack growth kinetics upon chondrite petrologic type by quantifying the percentage of cracked surface as a function of the number of cycles on a representative surface of the processed samples (Fig. 10), which generally extends for a few $mm^2$. A series of duplicate experiments on the different studied

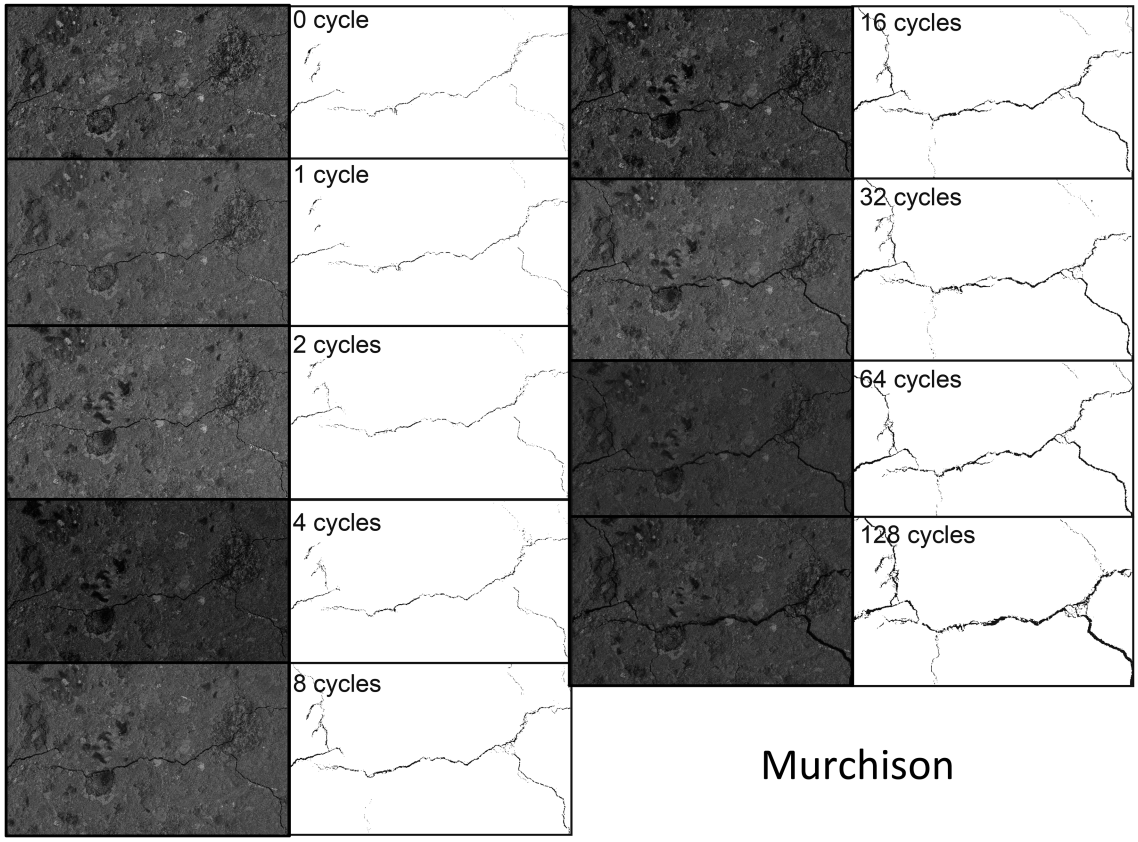


**Figure 5.** EDS–SEM images of crack growth on the surface of Murchison from 0 to 128 thermal cycles with $\Delta T \approx 280$ K and $T_{max.} \approx 583$ K. Size of the image: 1mm∗1.5 mm.

chondrites has been undertaken to evaluate the reproducibility of the crack growth rates. Duplicate experiments on two different samples of the Murchison chondrite (experiments 1 and 2, Fig. 10) show results in close agreement with each other (within uncertainties), indicative of similar growth rate at high number of cycles and efficiency to generate cracks during the first thermal cycles. Similarly, duplicate experiments on Allende samples at different number of cycles suggest that the crack growth rates can be extrapolated at large number of thermal cycles for CV chondrites. Finally, duplicate experiments on the Sahara 97 210 samples performed at $\Delta T \approx 280$ K for experiment 2 and at $\Delta T \approx 530$ K for experiment 1 reveal that increasing $\Delta T$ by almost a factor of 2 did not change significantly the crack growth rates for our ordinary chondrite representative sample.

Starting with a non-linear behaviour during first thermal cycles (which is expected from crack propagation theory, as shown by Delbo et al. 2014, in particular their extended data Fig. 7), the crack growth rate as a function of the number of cycles becomes almost constant suggesting that the propagation of cracks is still an active process at large numbers of cycles. Murchison crack growth rate upon thermal cycling is significantly larger than that recorded for both Allende and Sahara 97 210 (Fig. 10). The total area of crack width for Murchison exceeds 1 per cent after a limited number of cycles (8 cycles), whereas this amount is never achieved in both the Allende and Sahara 97 210 chondrites even after a few hundreds of cycles. Our results also show that crack growth is faster in Allende than in Sahara 97 210. A significant increase in the amplitude of the thermal variation ($\Delta T \approx 280$ K and $\Delta T = 530$ K; Table 1) barely affects the crack growth rate occurring in Sahara 97 210, which seems to step down after a few tens of thermal cycles. Such differences in crack growth between carbonaceous and ordinary chondrites are also consistent with the trend observed from our previous set of experiments (Delbo et al. 2014).

### 3.4 Potential particle production during thermal cycling experiments

As the number of thermal cycles increases, in this set of experiments we observe crack segments that lengthen, branch and, by their interconnectivity, define the outline of 2D fragments formed by thermal cracking (Figs 3, 4, 8, and 9). Despite their differences as mentioned above, the studied chondrites show after only a hundred of thermal cycles similar crack networks (Fig. 9). While some of the crack networks have irregular arrangement of cracks, their typical fabric is constituted by more or less irregular polygonal-like network structures delineated by 4–6 crack segments on average.

Since the potential of fragmentation of the starting chondrite material is increasing with the number of thermal cycles (Figs 5–7), no attempt has been made here to quantify in details the grain size distribution of potential chondrite fragments. It should be noticed that the larger 2D regions bounded by the network of cracks never appear to exceed the size range between 0.5 and 1 mm. X-ray tomography on Murchison and Allende samples allows us to evaluate the depth at which the cracks can penetrate within the samples (Fig. 11 and supplementary material). In general, cracks propagate in the chondrite almost perpendicular to the heated surface. For the Murchison sample, maximum depths of penetration of cracks are in the range of 250–400 μm after 100 thermal cycles and closer to 400–500 μm for Allende after 1500 thermal cycles (Fig. 9). The

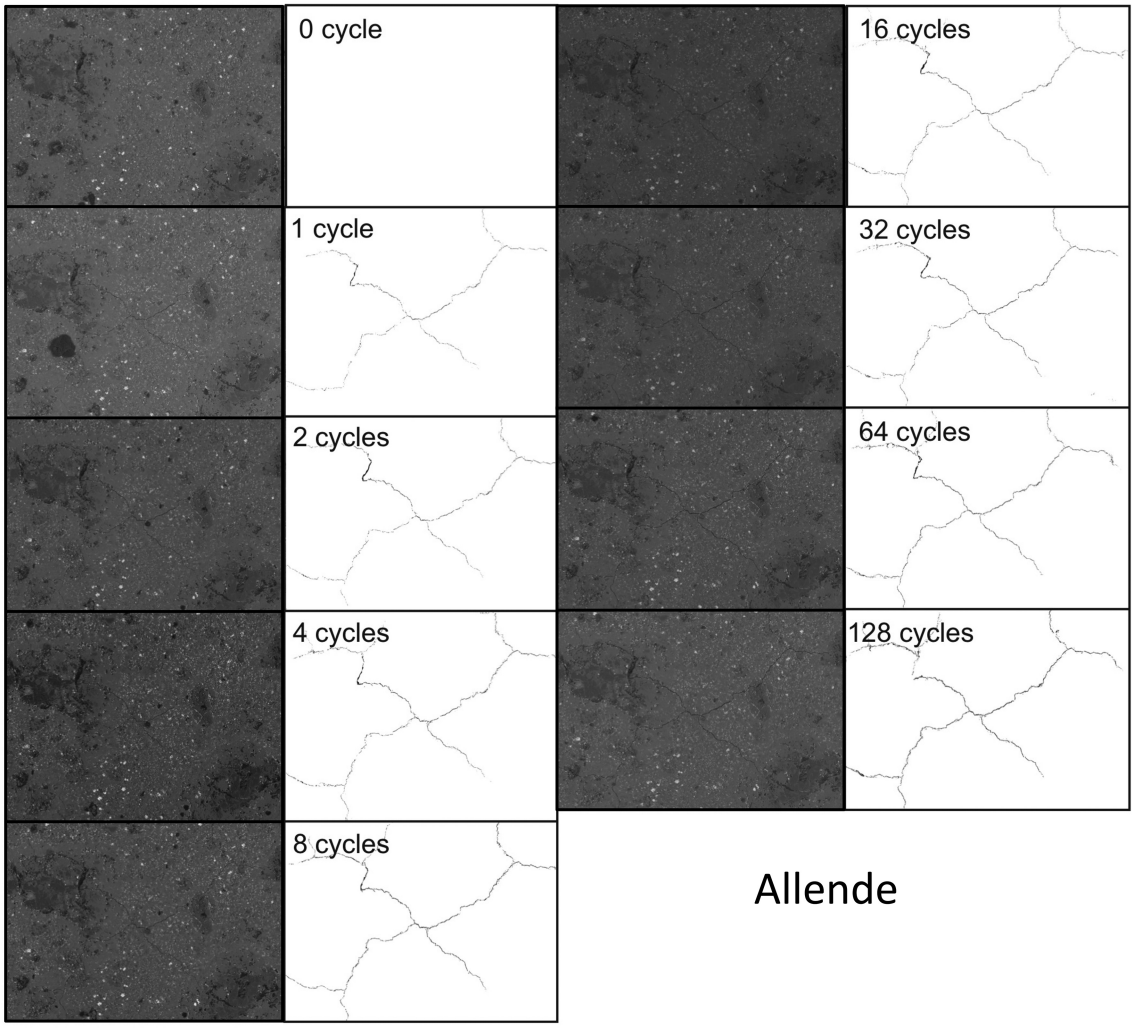


**Figure 6.** EDS–SEM images of crack growth on the surface of Allende sample from 0 to 128 thermal cycles (Table 1). Size of the image: 1.4mm∗2.1 mm.

combination of the 2D SEM images with their orthogonal X-ray tomography equivalents reveals that the particle size defined by the spatial characteristics of the crack network in Murchison and Allende is variable from a few tens of μm to 800–1000 μm with averaged size never exceeding 400–500 μm. The branching of the crack surfaces in 3D promotes the formation of 'potential' grains, which can be defined as a part of the material surrounded by totally damaged areas, mechanically free and relieved of any mechanical tension, but still trap in the sample by the crack geometry. These potential particles possibly resembling chondritic asteroid surface fragments may contribute to the formation of the regolith since they could detach and separate from the source rock by the interplay of micro-shaking and/or impacts of micrometeorites, etc.

## 4 DISCUSSION AND IMPLICATIONS

In our set of experiments, there is a correlation between the proportion of cracked surface (Fig. 10) and the mass-loss associated with the release of volatile from the samples (Fig. 2): from TGA measurements, mass-losses, mainly attributed to molecular water, are estimated around 3.26 wt per cent for Murchison, 2.18 wt per cent for Allende, and <0.1 wt per cent for Sahara 97 210, with no significant difference between experiments 1 and 2 (Table 1) for the latter meteorite (Fig. 10); by comparison, the proportion of cracked surface as determined by image processing reached 2.36 per cent for Murchison, 0.62 per cent for Allende, and 0.32 per cent for Sahara 97 210. Similarly, the larger width of the cracks developed in Murchison compared to those of the crack networks observed both in Allende and in Sahara 97 210 (Figs 8 and 9) could be a response to the larger abundance of hydrated phases in Murchison, and to the significant volume decrease due to the incremental dehydration imposed by the thermal cycles. Indeed dehydration has been shown not only to change the mass of a specimen, due to volatile release, but also affect the volume of the silicates: heating of CM/CI chondrites (Nozaki Nakamura & Noguchi 2006; Nakato et al. 2008; Garenne et al. 2014) and experimental heating of phyllosilicate standards (Che & Glotch 2012; Garenne et al. 2014) have shown that evaporation of adsorbed/interlayer water in phyllosilicates on heating at ∼500 K causes silicate sheets to contract; this is referred to as dehydration (Drits & McCarty 2007).

It comes, taking a phyllosilicate-rich chondrite like Murchison as an example, that during each short thermal pulse (incremental dehydration), the sheet silicate interlayer water is progressively lost, giving rise to tensile stresses. Even if the exact rheology of

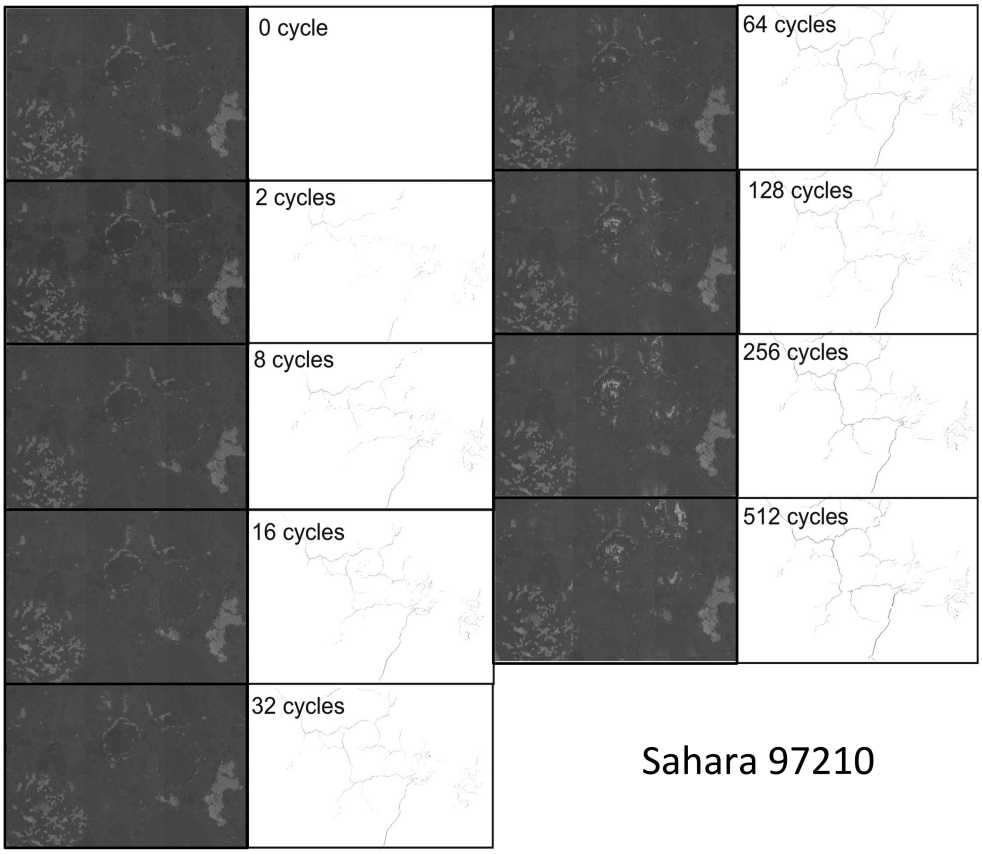


**Figure 7.** EDS–SEM images of crack growth on the surface of Sahara 97 210 from 0 to 512 thermal cycles with $\Delta T \approx 530$ K and $T_{max.} \approx 713$ K. Size of the image: 2mm∗3 mm.

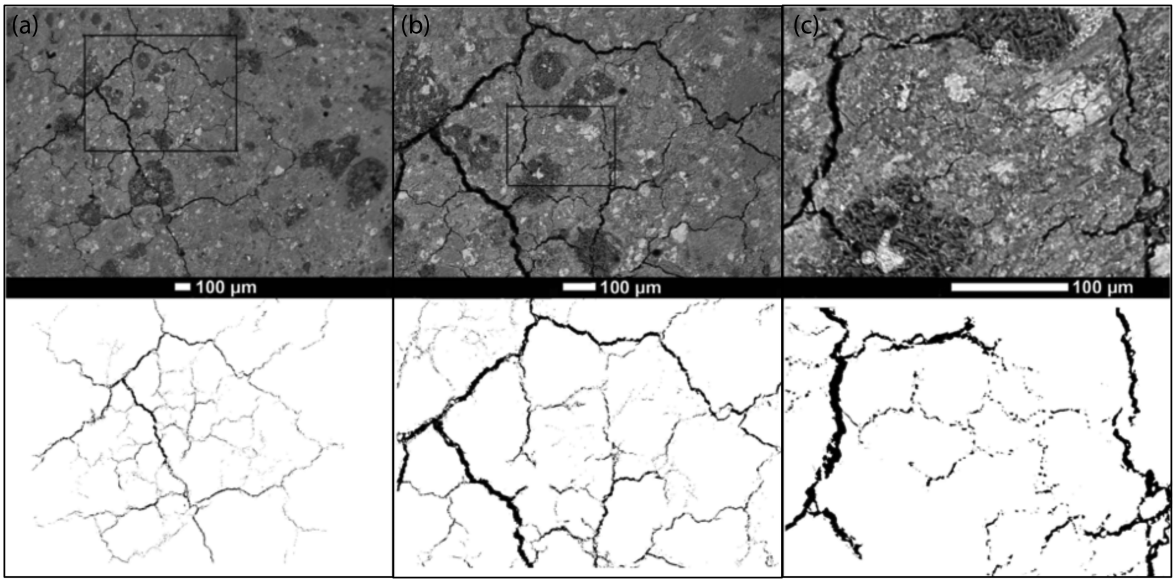


**Figure 8.** EDS–SEM images of the surface of Murchison (CM2) after 100 thermal cycles showing the branching of crack segments at different scales, e.g. fractal-like characteristics. Opening of the cracks in Murchison pulse heated sample is large up to 40–50 µm. The interconnectivity of crack segments defines the outline of polygonal-like crack network.

dehydrating rocks yet remains to be determined, experiments have shown that dehydration reactions can induce strain and/or stress concentrations that are relieved by the formation of microcracks, grain boundary opening, and by a newly formed porosity (Drits & McCarty 2007; Brantut et al. 2012), which in our case results in the formation of a characteristic pattern of open cracks on the free surface of the chondrite, as we observed it (Fig. 8). In a sense, these networks of open cracks are similar to desiccation polygonal

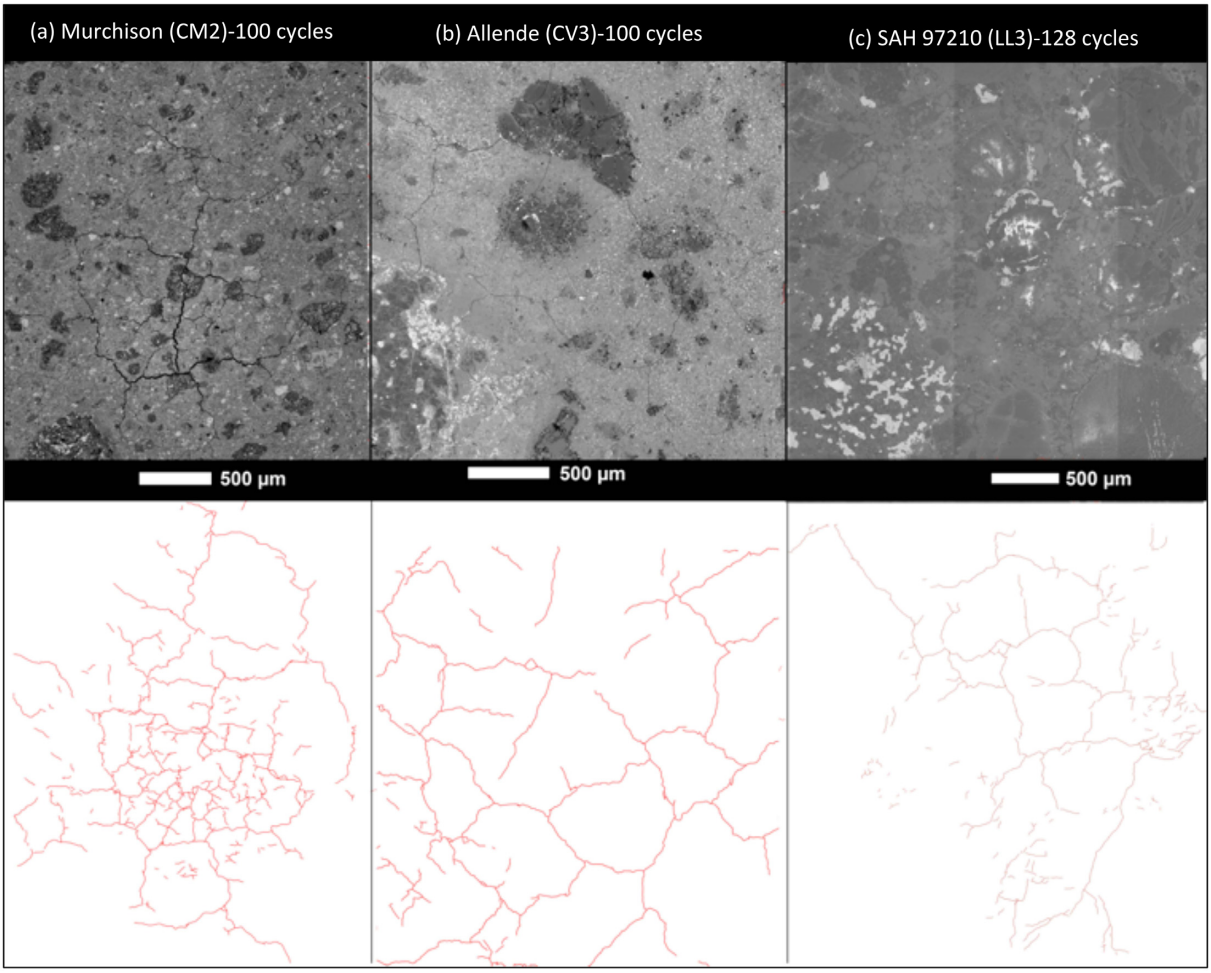


**Figure 9.** Comparison of damages at the surface of Murchison, Allende and Sahara 97 210 resulting from ≈ 100 thermal cycles. The width of drawn lines representing the crack network for each sample is not representative of the effective opening/width of the real cracks. On average, crack width increases drastically from Sahara 97 210 (< 5 µm), Allende (≈ 5–10 µm), and Murchison (up to 40–50 µm).

structures originating as shrinkage cracks formed by the evaporation of water from the surface of clay-rich sediment. Also known as mud cracks, they are of subaerial origin, and are caused by the slow drying-out of muddy sediments, which have been exposed to the repeated action of sun and wind (Velde 1999).

This analogy, especially for the laser pulse heated Murchison samples, may provide a physical background to understand the observed polygonal patterns (Goehring 2013). But how far we can push this comparison would necessitate a dedicated study. On the other hand, the work of Delbo et al. (2014), based on heating cycles below the dehydration/dehydroxylation temperatures also showed that Murchison experiences a larger crack growth than Sahara 97 210. This indicates that the different crack growths of the two meteorites can also be due to their different thermo-mechanical properties and not only due to the release of water.

If dehydration were indeed the only important mechanism for promoting shrinkage cracks in hydrated chondrites such as CM and CV, the occurrence of crack networks in Sahara 97 210 (Fig. 9) would not necessarily be similar to those observed in the two carbonaceous chondrites. On the contrary also the anhydrous meteorite shows similar crack pattern to those observed in the Murchison. This result indicates that the establishment and growth of a network of cracks is not only due to dehydration, but it must be related to a phenomenon occurring on chondrites, and their source asteroids, in general. We speculate here that dehydration increases the nucleation and propagation of these networks of cracks. In chondrites in which hydrous phases are lacking or rare, crack propagation must be essentially related to the activation of previous generation of flaws, such as microcracks at grain or clivage boundaries, and cracks according to the Griffith criterion for crack extension (Griffith 1920). Griffith proposed that a brittle material contains a population of fine small cracks and flaws that have a variety of sizes, geometries, and orientation that produces a stress concentration of sufficient magnitude so that the theoretical cohesive strength is reached in localized regions at a nominal tensile stress that is well below the theoretical value, and here equal to the one imposed by each incremental thermal cycle. Fracture propagation in a 'dry' material such as Sahara 97 210 is thus possible as a result of conversion of elastic strain energy into fracture surface energy, leading to crack (polygonal-like) networks as crack segments lengthen and branch due to the random distribution of the pre-existing generation of small cracks and flaws.

It is thus very likely that crack extension by the activation of previous generation of flaws and cracks will be efficient for establishing a network of thin cracks in the upper part of any asteroid surface subject to diurnal temperature variations (Fig. 9).

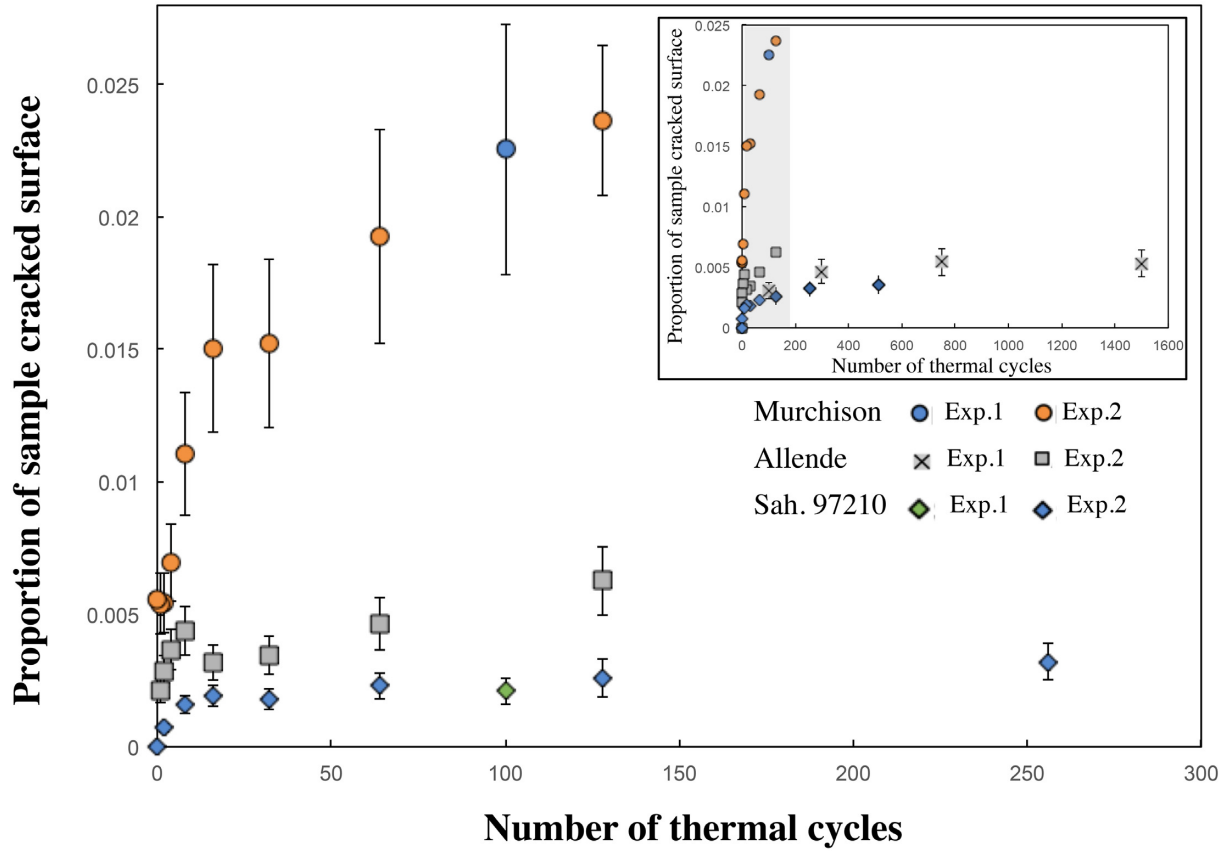


**Figure 10.** Evolution of the measured proportion of sample cracked surface versus number of thermal cycles for Murchison, Allende, and Sahara 97 210 exposed to thermal cycling. Experimental conditions (experiments 1 and 2) are those indicated in Table 1. The insert shows results obtained for the greatest number of cycles. The shaded area represents data obtained for data for the first 128th cycles.

Dehydration, if it occurs, will enhance the process by favouring shrinkage cracks from the previous generation of flaws/cracks and the opening of large voids between the crack walls (Figs 4 and 8). In the case of higher thermal variations (Fig. 2), severe contraction and damage are expected due to partial or total dehydroxylation of the phyllosilicates.

Our results indicate that the surface of the chondrite/asteroid specimens that are exposed to thermal cycles develops network of cracks. These cracks can have depths in the subsurface up to several hundreds of microns. We suspect that the depth of the cracks is directly related to the heat penetration depth, as shown by El Mir Ramesh & Delbo (2019). In temperature cycles, the heat wave typically penetrates in the subsurface by a length $l_S = (kP/(2\pi\rho C))^{1/2}$, where K, $\rho$, and C are the material thermal conductivity, density, and specific heat, respectively, whereas P is the spin period of the body. The value of $l_S$ is of a few cm for typical values of K, $\rho$, and C of chondrites (Opeil Consolmagno & Britt 2010; Opeil et al. 2012, 2020) and spin periods of a few hours, which are typical of asteroids. However, for the thermal cycles studied here, where P < 1 min, the value of $l_S$ could be around 1 mm, in global agreement with 3D views (Figs 11 and 12 and supplementary material).

A significant increase of the local surface porosity in the first few millimetres or centimetres – depending on the temperature cycles' period – is expected as a result of thermal cycling, irrespective of the nature of the meteorite type studied here. We note that using the scaling laws of El Mir et al. (2019) this would indicate increasing in porosity for a few cm in the subsurface of asteroid rocks. It is indeed observed that the surfaces of the boulders on Ryugu and Bennu have substantially higher porosities compared to the meteorites supposedly of the similar composition (Grott et al. 2019; Okada et al. 2020; Rozitis et al. 2020). Thermal conductivity being in turn dependent on area according to Fourier law of heat conduction, the present results suggest that alteration of the superficial porosity of asteroid surfaces due to diurnal temperature variations may influence significantly the thermal inertia (see also Delbo et al. 2015 and Okada 2016).

It is worth keeping in mind however that crack pore space should not be confused with bulk porosity in the parent material. As a consequence, incremental dehydration, and thermal cycles due to diurnal temperature variations make an asteroid surface more porous and thus friable (see also Suttle et al. 2017). This may be responsible for the uprooting and the split-up of grains from the parent rock, which in turn may contribute to the formation of dust particles and eventually to the regolith. We have already observed fragments that broke off from an unprepared chunk of Murchison after temperature cycling (Delbo et al. 2014; Fig. 3). However, we did not observe any particle extracted from the surface of our samples from this set of experiments, even if we do observe potential grains delineated by crack networks (Fig. 8). This is probably due to the number of cycles that was not large enough to provoke crack growth covering a substantial fraction of the size of the samples. To be detached and contribute to the formation of regolith, grains need to be isolated by cracks not only on surface but also at depth (Fig. 12). Such cracks are not favoured by the flat and polished surfaces we worked with, but

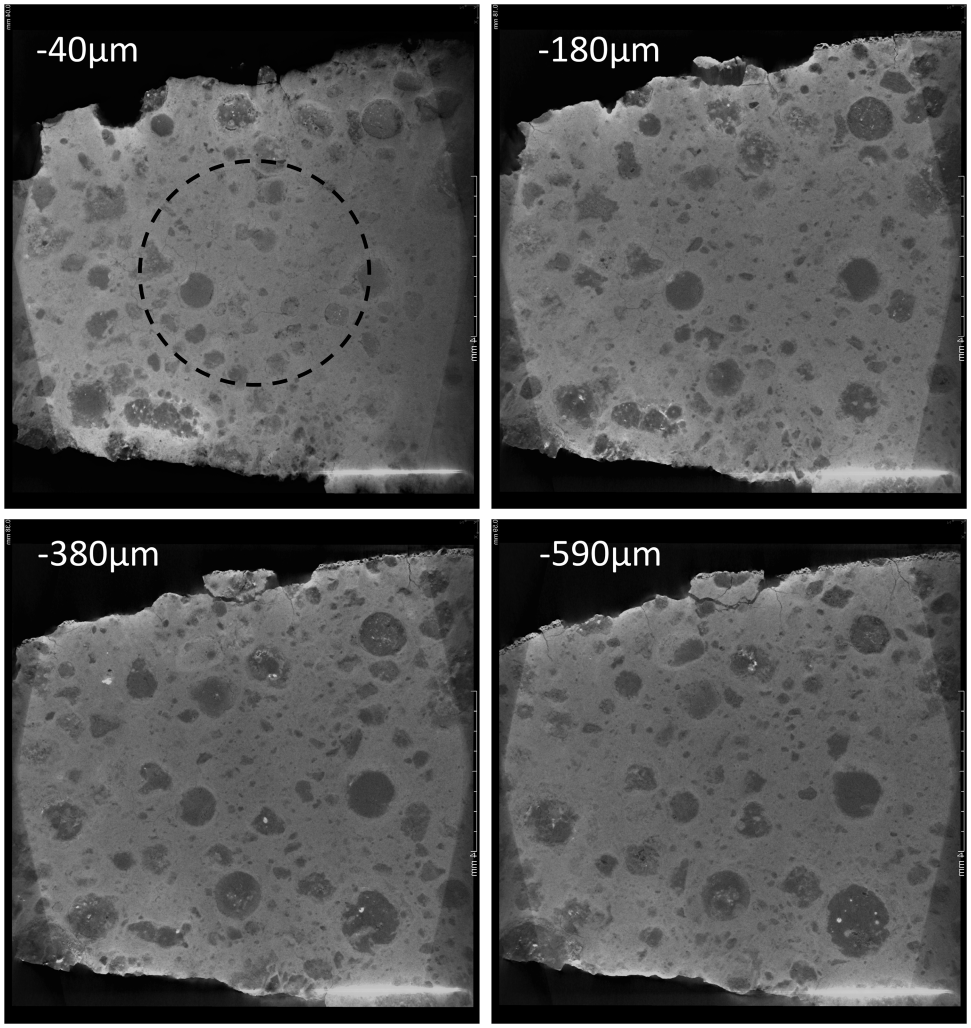


**Figure 11.** 3D X-ray tomography section images of Allende sample after 1000 thermal cycles taken at different depth below the surface of the specimen (see Fig. 3). The dashed circle corresponds approximately to the location of the beam on the surface of the sample. Note that most of the cracks have disappeared at a depth of 400–500 µm below the surface. See supplementary material.

should exist in natural samples. Asteroids have generally rough surfaces, which may facilitate the extraction of protruding particles. In addition, they also provide local environments favourable for cracks propagation with high dT/dt due to shadowing effects (Ali-Lagoa et al. 2015). Nevertheless, these thermal cycling experiments (Fig. 9) show unambiguously that shrinkage cracks driven by dehydration processes are the more prone to isolate and unseal grains from a chondritic matrix, showing the importance of the modal abundance of their phyllosilicate and hydrated phases. For a large number of thermal cycles, grain unsealing will be the easiest for Murchison, less easy to difficult for Allende and hard for Sahara 97 210. This process is of prime importance for micrometeorites formation and will be addressed in a forthcoming paper.

Our experiments are relevant for the cracking of asteroids near the sun (Marchi et al. 2009; Granvik et al. 2016), in particular for the active asteroid (3200) Phaethon (Jewitt Li & Agarwal ), which is the target of the JAXA fly-by mission Destiny+ (Arai et al. 2018). Phaethon is the parent body of the Geminids, one of the most predominant meteor streams. Several studies (de Leon et al. 2010; Todorovic 2017, 2018) show that Phaethon is likely originating from the family of asteroids associated with (2) Pallas, one of the largest members of the Main Belt. Pallas is clearly hydrated (Usui et al. 2019 and references therein) while Phaethon is not (Kareta et al. 2018). Pallas has a composition that makes CM chondrites the best meteorite analogue, as indicated by Pallas' near infrared spectrum and by the strong hydration band at 2.7 µm. The bulk density of Pallas is also compatible with the bulk density of CM (Marsset et al. 2020). Hence, it is very likely that Phaethon has lost its hydration by its close approaches to the sun at 0.14 au, where the surface reaches temperatures of about 1000 K. By analogy with our experiments, we thus expect a process of dehydration (and dehydroxylation) and cracking of the surface of this asteroid as shown by the Murchison specimen. It is thus conceivable that a combination of thermal and dehydration/dehydroxylation cracking process is at the origin of the materials released from Phaethon. This process is likely to affect all other low-perihelion near the Earth asteroids with originally hydrated composition.

## 5 CONCLUSIONS AND PLANETARY PERSPECTIVES

We show that carbonaceous and ordinary chondrite meteorites display well-developed crack networks when submitted to laser-induced

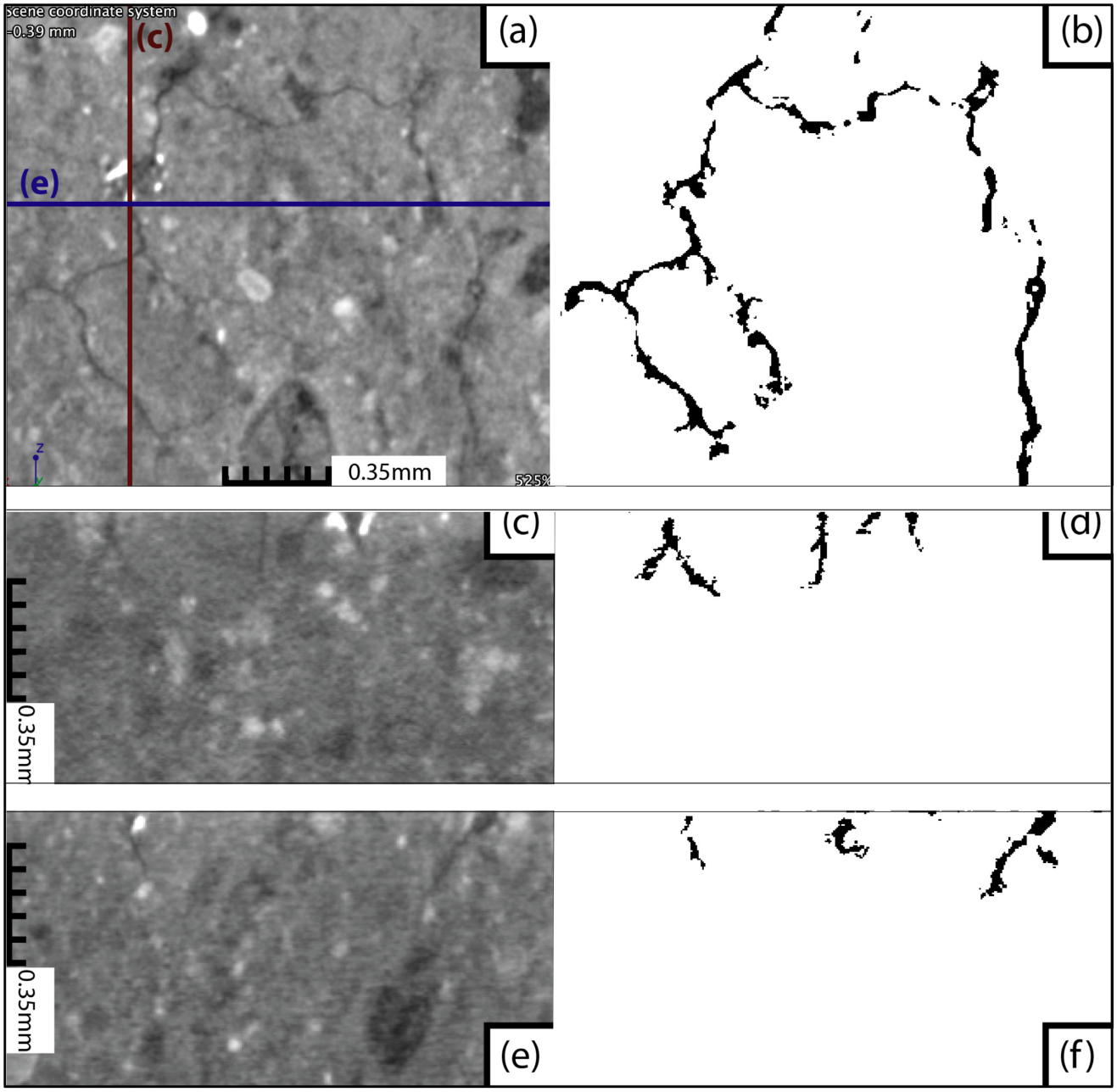


**Figure 12.** X-ray tomography of the subsurface of Murchison sample after 100 thermal cycles (Table 1). Upper images show the surface and the two lower ones the orthogonal vertical sections. The interconnectivity of crack segments defines the outline of a polygonal-like crack network at the surface (see also Figs 8 and 9) that propagate in the subsurface (see text). The branching of the crack plans in 3D promotes the formation of potential grains, i.e. part of the material surrounded by totally damaged areas, mechanically free (relieved of any mechanical tension), but still trap in the sample by the crack geometry.

thermal cycling experiments. This set of experiments demonstrates that thermal cycling is an efficient mechanism to activate pre-existing generations of flaws and cracks favouring cracks propagation. As cracks propagate, crack segments lengthen, branch and, by their interconnectivity, define the outline of the polygonal-like crack networks in both carbonaceous and ordinary chondrite samples. X-ray tomography of the pulse heated samples reveals the formation of potential grains delineated by the crack network, which may contribute to the regolith by unsealing. It is shown that the average grain size after $10^2$–$10^3$ thermal cycles never exceeds 400–500 µm in both carbonaceous and ordinary chondrite samples. Significant differences concerning the formation of crack networks by thermal cycling experiments exist however between the different types of studied chondrites, which can be related to the modal abundances of phyllosilicates and hydrated phases of the unheated samples. For the range of temperature investigated here (up to 583 K), incremental dehydration due to thermal cycling is shown to favour the development of shrinkage cracks and the opening of large pores. The sheet silicate interlayer water is progressively lost giving rise to tensile stresses that are relieved by the formation of a characteristic pattern of open cracks on the free surface of the chondrite, e.g. Murchison. This set of experiments also reveals a clear correlation

between the proportion of surface cracked or the surface porosity, and the mass-loss associated with the release of volatile from the samples and/or the modal abundance of phyllosilicates.

In planetary perspective, these proof of concept-like experiments demonstrate that incremental dehydration due to diurnal temperature variations on near-Earth asteroids alter significantly their outer layer porosity and thermal conductivity. This could explain the higher-than-expected porosity measured for the most abundant type of rocks on the rugged surface of Ryugu and Bennu. Because diurnal temperature variations make the asteroid surface more friable, carbonaceous chondritic asteroids that have close approaches to the Sun, as the asteroid (3200) Phaethon, should experience extensive surface material cracking due to the additive effect of both dehydration and deshydroxylation of their hydrous phases. We speculate that if the potential fragments defined by the crack network are actually produced, they could contribute to the activity of these bodies.

## ACKNOWLEDGEMENTS

This paper is based on the experimental work done by MN during a 1 yr post-doc position at the Laboratoire Énergies & Mécanique Théorique et Appliquée (Université de Lorraine) and CRPG (Université de Lorraine) under the supervision of BR, MD, and GL and financially supported by the French Agence National de la Recherche (ANR-11-BS56–008: SHOCKS; MD Principal investigator). MD and the authors wish to acknowledge the French Agence National de la Recherche (ANR) SHOCKS, the BQR of the Observatoire de la Côte d'Azur (OCA), the University Côte d'Azur, the Laboratory GeoAzur, and the French National Program of Planetology (PNP/INSU,CNRS). GL, MD, and PM also acknowledge funding support from the French space agency CNES as science team co-investigators of the NASA OSIRIS-REx asteroid sample return mission, as well as from Academies of Excellence: Complex systems and Space, environment, risk, and resilience, part of the IDEX JEDI of the Université Côte d'Azur. PM acknowledges funding support from the European Union Framework Programme for Research and Innovation under grant agreement No. 870377 (project NEO-MAPP). Finally, the authors wish to thank Christophe Morlot (SCMEM, Université de Lorraine) for his help in collecting X-ray 3D tomography analyses, Daniel Pino Munoz (CEMEF, Mines ParisTech, Valbone) for numerous scientific discussions, Kavan Hazali for his review which substantially improved the quality of this manuscript, and the associate editor for editorial handling.

Author contributions are summarized as follows: GL and MD designed the project, MN supervised by BR and GL carried out the laser experiments, LA carried out the analyses of TGA, CG processed the raw data and performed with GL the figures. GL, CG, PM, MD, BR, and MN interpreted the data and contributed to data analysis. GL, CG, and MD wrote the manuscript.

## DATA AVAILABILITY

The data underlying this article will be shared on reasonable request to the corresponding author.

## REFERENCES

Alí-Lagoa V., Delbo M., Libourel G., 2015, ApJ, 810, L22
Arai T., Kobayashi M., Ishibashi K. et al., 2018, LPSC, 49, 2570
Arakawa et al., 2020, Science, 368, 67
Attree N. et al., 2018, A&A, 610, A76
Auger A. T. et al., 2018, Icarus 301, 173
Brantut N., Schubnel A., David E. C., Héripré E., Guéguen Y., Dimanov A., 2012, Journal of Geophysical research , 117, B03205
Britt D. T., Consolmagno S. J. G. J., 2003, Meteoritics, 38, 1161
Che C., Glotch T. D., 2012, Icarus, 218, 585
Collins B. D., Stock G. M., 2016, Nature Geoscience, 9, 395
Collins B. D., Stock G. M., Eppes M. C., Lewis S. C., Corbett S. C., Smith J. B., 2018, Nature Communications, 9, 762
Delbo M., Mueller M., Emery J. P., Rozitis B., Capria M. T., 2015, Asteroids IV, 107
Delbo M. et al., 2014, Nature, 508, 233
De León J., Campins H., Tsiganis K., Morbidelli A., Licandro J., 2010, A&A, 513, A26
Dombard A. J., Barnouin O. S., Prockter L. M., Thomas P., C. 2010, Icarus, 210, 713
Drits V. A., McCarty D. K., 2007, Clays Clay Miner., 55, 45
El-Maarry M. R. et al., 2015, Geophys. Res. Lett., 42, 5170
El Mir C., Ramesh K. T., Delbo M., 2019, Icarus, 333, 356
Eppes M. C., Willis A., Molaro J., Abernathy S., Zhou B., 2015, Nature Communications, 6, 6712
Garenne A., Beck P., Montes-Hernandez G., Chiriac R., Toche F., Quirico E., Bonal L., Schmitt B., 2014, Geochim. Cosmochim. Acta., 137, 93
Gibson E. K, Jr, 1976, Meteoritics, 11, 286
Goehring L., 2013, Philos. Trans. R. Soc. A Math. Phys. Eng. Sci., 371, 20120353
Granvik M. et al., 2016, Nature, 530, 303
Griffith A. A., 1920, Phil. Trans., 221,163
Grott M. et al., 2019, Nat. Astron., 3, 971
Gundlach B., Blum J., 2013, Icarus, 223, 479
Hazeli K., El Mir C., Papanikolaou S., Delbo M., Ramesh K. T., 2018. Icarus, 304, 172
Heiken G., McKay D. S., 1974, Lunar Science Conference Vol. 1, 5th, Houston, Tex., March 18–22, 1974, Proceedings. Pergamon Press, Inc., New York, p. 843
Housen K. R., Holsapple K. A., 2011, Icarus. 211, 856
Housen K. R., Wilkening L. L., Chapman C. R., Greenberg R., 1979, Icarus, 39, 317
Howard K. T., Benedix G. K., Bland P. A., Cressey G., 2009, Geochim. Cosmochim. Acta, 73, 4576
Howard K. T., Benedix G. K., Bland P. A., Cressey G., 2010, Geochim. Cosmochim. Acta, 74, 5084
Hörz F., Cintala M., 1997, Meteoritics, 32, 179
Kareta T. et al., 2018, AJ, 156, 287
Lauretta D. S. et al., 2019, Science, 366, eaay3544
Liang B., Cuadra J., Hazeli K., Soghrati S., 2020, Icarus, 335, 113381
Marchi S., Delbo M., Morbidelli A., Paolicchi P., Lazzarin M., 2009, MNRAS, 400, 147
Marsset M. et al., 2020, Nature Astronomy, 4, 569
Miyamoto et al., 2007, Science, 316, 1011
Molaro J. L., Byrne S., Langer S. A., 2015, J. Geophys. Res. Planets, 120, 255
Molaro J. L., Byrne S., Le J L., 2017, Icarus, 294, 247
Molaro J. L. et al., 2020, Nat. Commun., 11, 2913
Nakato A., Nakamura T., Kitajima F., Noguchi T., 2008, Earth Planets Sp., 60, 855
Nozaki W., Nakamura T., Noguchi T., 2006, Meteoritics, 41, 1095
Okada T., 2016, 47th Lunar and Planetary Science Conference, p. 1457
Okada T. et al., 2020, Nature, 579, 518
Opeil C. P., Britt D. T., Macke R. J., Consolmagno G. J., 2020, Meteoritics, in press
Opeil C. P., Consolmagno G. J., Britt D. T., 2010, Icarus, 208, 449
Opeil C. P., Consolmagno G. J., Safarik D. J., Britt D. T., 2012, Meteoritics, 47, 319
Pajola M. et al., 2017, Nat. Astron., 1, 0092
Pohl L., Britt D. T., 2020, Meteoritics, 55, 962
Ravaji B., Ali-Lagoa V., Delbo M., Wilkerson J. W., 2019, J. Geophys. Res., 124, 3304
Richter D., Simmons G., 1974, Int. J. Rock Mech. Min. Sci., 11, 403
Rozitis B. et al., 2020, Science, 6, eabc3699

Ruesch O. et al., 2020, Icarus, 336, 113
Slyuta E. N., 2017. Sol. Syst. Res., 51, 64
Suttle M. D., Genge M. J., Folco L., Russell S. S., 2017, Geochim. Cosmochim. Acta, 206, 112
Svetsov V. V., Nemtchinov I. V, Teterev A. V., 1995, Icarus, 116, 131
Todorovic N., 2017, MNRAS, 465, 4441
Todorovic N., 2018, MNRAS, 475, 601
Tsuchiyama A., Mashio E., Imai Y., Noguchi T., Miura Y. N., Yano H., 2008, Japan Geosciences Union Meeting, Abstracts of Papers, Chiba, no. P168–P002
Usui F., Hasegawa S., Ootsubo T., Onaka T., 2019, PASJ, 71, 1
Velde B., 1999, Geoderma, 93, 101
Veverka J. et al., 2001, Nature, 413, 390
Viles H., Ehlmann B., Wilson C. F., Cebula T., Page M., Bourke M., 2010, Geophys. Res. Lett., 37, L18201
Vincent J. - B., Besse S., Marchi S., Sierks H., Massironi M., the OSIRIS-Team, 2012. Planet. Space Sci., 66, 79
Vincent J. - B. et al., 2015, Nature, 523, 63
Walsh K. J. et al., 2019, Nat. Geosci., 12, 242
Watanabe S. et al., 2019, Science, 364, 268
Yano H. et al., 2006, Science, 312, 1350

## SUPPORTING INFORMATION

Supplementary data are available at *MNRAS* online.

**Figure S1.** Example of 3D X-ray tomography movie (.mp4) for Allende sample, experiment 2, 128 cycles (see Table 1), showing the subsurface crack networks. Most of the cracks have disappeared at a depth of 400–500 μm below the surface (see slow motion part).

Please note: Oxford University Press is not responsible for the content or functionality of any supporting materials supplied by the authors. Any queries (other than missing material) should be directed to the corresponding author for the article.

This paper has been typeset from a Microsoft Word file prepared by the author.